

# Strain Enhanced Visible–Ultraviolet Absorption of Blue Phosphorene/MoX<sub>2</sub> (X = S, Se) Heterolayers

Di Gu, Xiaoma Tao, Hongmei Chen, Yifang Ouyang,\* Weiling Zhu, Qing Peng,\* and Yong Du

With ultrahigh carrier mobility and large band gap, blue phosphorene (bP) is a promising photoelectronics surpassing black phosphorene and can be further improved by heterostacking. Herein, strain-engineering of the electronic band gaps and light absorption of two van der Waals heterostructures bP/MoS<sub>2</sub> and bP/MoSe<sub>2</sub> via first-principles calculations has been reported. Their electronic band structures are sensitive to in-plane strains. It is interesting and beneficial that biaxial compressive strain range of  $-0.02$  to  $-0.055$  induces the direct band gap in bP/MoSe<sub>2</sub>. There are two critical strains for bP/MoS(Se)<sub>2</sub> heterostructures, where the semiconductor–metal transition can be observed. The bP/MoS(Se)<sub>2</sub> heterostructures exhibit strong visible–ultraviolet light absorption, which can be further enhanced via biaxial strain. Our results suggest that bP/MoS(Se)<sub>2</sub> heterostructures have promising electronics and visible–ultraviolet optoelectronic applications.

Graphene, as a two-dimensional (2D) atomically thin material, has attracted a great of attention since its discovery in 2004.<sup>[1]</sup> Unlike a general semiconductor, graphene has no gap between its valence and conduction bands, which limits its electronic applications.<sup>[2,3]</sup> As alternatives of graphene, the transition metal dichalcogenides (TMDs), such as MoS<sub>2</sub> and MoSe<sub>2</sub>, were

reported that they had sizable bandgap, advantageous optoelectronic and distinguished mechanical properties.<sup>[4–7]</sup> Especially, both of monolayer MoS<sub>2</sub> and MoSe<sub>2</sub> are of direct band gap which is suitable for electronic or optoelectronic applications.<sup>[5,8–10]</sup> Phosphorus was reported as another class of 2D material beyond graphene and transition metal dichalcogenides.<sup>[11–14]</sup> The transport properties of black phosphorus are prominent.<sup>[15]</sup> For example, the electron carrier mobility of monolayer black phosphorus is high up to  $1000\text{ cm}^2\text{ V}^{-1}\text{ s}^{-1}$ ,<sup>[12]</sup> which is higher than the electron carrier mobility of semimetallic graphene and monolayer MoS<sub>2</sub> ( $10\text{--}200\text{ cm}^2\text{ V}^{-1}\text{ s}^{-1}$ ). Similar to black phosphorus, blue phosphorene (bP), which could be converted from the black phos-

phorene by certain dislocation of constituent P atoms, is another allotrope of phosphorene.<sup>[13,16–19]</sup> Recently, bP was predicted by the theoretical calculations with a higher hole mobility about  $1800\text{ cm}^2\text{ V}^{-1}\text{ s}^{-1}$  and a larger bandgap of  $\approx 2.0\text{ eV}$  than black phosphorene.<sup>[16,19,20]</sup>


Due to the fact that the application of the 2D material was limited by single material system with restricted properties, many researchers tried to vertically stack two different 2D materials to achieve van der Waals (vdW) heterostructures via vdW interaction.<sup>[21–23]</sup> Recent studies have shown that vdW heterostructures would be a facile way to achieve advanced properties by combination of different monolayers 2D materials.<sup>[24–29]</sup> For example, Deng et al.<sup>[30]</sup> reported that a gate-tunable P–N diode based on a P-type black phosphorus and a N-type monolayer MoS<sub>2</sub> as a photodetector, which showed a photodetection responsivity of  $418\text{ mA W}^{-1}$  and was much higher than the value of  $4.8\text{ mA W}^{-1}$  for the single black phosphorus phototransistors. Ganesan et al.<sup>[31]</sup> demonstrated theoretically that phosphorene and TMDs heterostructures would be suitable for excitonic thin film solar cell applications. The black phosphorus and MoS<sub>2</sub> vdW heterostructure possessed good piezoelectric effect via the compressive strain.<sup>[32]</sup> Moreover, it was worth to note that bP shared a similar hexagonal crystal structure and nearly identical lattice constants with MoS<sub>2</sub> and MoSe<sub>2</sub>. From the point view of lattice match, bP would be more feasible to stack vdW heterostructures with MoS<sub>2</sub> and MoSe<sub>2</sub> than black phosphorene. Therefore, it is thus interesting to investigate the electronic and optical properties of bP/MoS(Se)<sub>2</sub> vdW heterostructures.

Dr. D. Gu, Prof. X. Tao, Prof. H. Chen, Prof. Y. Ouyang  
Guangxi Colleges and Universities Key Laboratory of Novel Energy  
Materials and Related Technology  
College of Physical Science and Technology  
Guangxi University  
Nanning 530004, P. R. China  
E-mail: ouyangyf@gxu.edu.cn

Dr. D. Gu, Prof. W. Zhu  
Department of Physics  
School of Science  
Guangdong University of Petrochemical Technology  
Maoming, Guangdong 525000, P. R. China

Dr. Q. Peng  
Department of Nuclear Engineering and Radiological Science  
University of Michigan  
Ann Arbor, MI 48109, USA  
E-mail: qpeng.org@gmail.com

Prof. Y. Du  
State Key Laboratory of Powder Metallurgy  
Central South University  
Changsha 410083, P. R. China

 The ORCID identification number(s) for the author(s) of this article can be found under <https://doi.org/10.1002/pssr.201800659>.

DOI: 10.1002/pssr.201800659

In this work, the equilibrium geometry of the stable bP/MoS(Se)<sub>2</sub> vdW heterostructures was constructed, and then the effect of different strain on the electronic and optical properties of bP/MoS(Se)<sub>2</sub> vdW heterostructures were investigated by using density functional theory (DFT).

In order to construct stable hybrid bP/MoS(Se)<sub>2</sub> vdW heterostructures, monolayer MoS<sub>2</sub>, MoSe<sub>2</sub>, and bP were relaxed firstly, and the values of lattice constants were, respectively, 3.169, 3.319, and 3.278 Å, which were in consistent with the previous reported data.<sup>[9,15]</sup> Six possible stacking configurations of bP/MoS(Se)<sub>2</sub> vdW heterostructures, as shown in **Figure 1(a)–(f)** namely A1-, A2-, A3-, B1-, B2-, and B3-stacking, were considered. For the A1-stacking, the top layer bP was directly stacked on the bottom layer MoS<sub>2</sub> or MoSe<sub>2</sub>, where the underneath P atom was just above the S or Se atom, and the three other upper P atoms were just located in the center of the adjacent three puckered hexagon of the bottom layers MoS(Se)<sub>2</sub>, respectively. The A2-stacking and the A3-stacking could be viewed as that the top layer bP of the A1-stacking was kept fixed, and the bottom layer MoS(Se)<sub>2</sub> of the A1-stacking was shifted along the armchair direction by 1/3 or 2/3 length of the cell, respectively. As a result, for the A2-stacking, the underneath P atom was just above the Mo atom and the upper P atoms were just above the S or Se atoms, where the edge of the puckered hexagon of the bottom layer MoS(Se)<sub>2</sub> and the edge of the puckered hexagon of the top layer bP were overlapping nicely. For the A3-stacking, the underneath P atom was just located in the center of the puckered hexagon of the bottom layer MoS(Se)<sub>2</sub>, and the three other upper P atoms were just above the Mo atoms. For the B1-, B2-, and B3-stacking, the MoS(Se)<sub>2</sub> were along

opposite direction. Analogously, the B2-stacking and the B3-stacking could be viewed as the bottom layer MoS(Se)<sub>2</sub> of the B1-stacking was shifted along the armchair direction by 1/3 or 2/3 length of the cell, respectively. Moreover, the B1-, B2-, and B3-stacking could also be viewed as that the bottom layer MoS(Se)<sub>2</sub> were rotated 180 degrees from A3-, A1-, and A2-stacking, respectively. All of the six stacking configurations were fully relaxed for getting stable atomic configuration.

The energy difference  $\Delta E_i$  (eV) is the difference between the energies of optimized bP/MoS(Se)<sub>2</sub> heterostructures and the most stable heterostructure (A2). As shown in **Figure 1(g)**, the trends of  $\Delta E_i$  between bP/MoS<sub>2</sub> and bP/MoSe<sub>2</sub> vdW heterostructures are very similar, especially both the  $\Delta E_i$  of B2-stackings were the largest, while those of the A2-stackings were the lowest. This indicates that the most stable structure is A2-stacking. As shown in **Figure 1(h)**, the A2-stackings were chosen as the optimum stacking order in the bP/MoS(Se)<sub>2</sub> vdW heterostructures. The interlayer distance ( $d$ ) of the bP/MoS(Se)<sub>2</sub> were estimated to be about 3.11(3.20) Å, which were in consistent with the previous reported data of vdW heterostructures.<sup>[33]</sup> The calculated optimal lattice parameters of bP/MoS<sub>2</sub> and bP/MoSe<sub>2</sub> vdW heterostructure were 3.223 and 3.298 Å, respectively. Compared with the lattice parameters of monolayer MoS(Se)<sub>2</sub> and monolayer bP, the lattice mismatches for bP/MoS<sub>2</sub> and bP/MoSe<sub>2</sub> vdW heterostructures were about 3.32 and 1.24%, respectively, both of them were in an acceptable range.

The electronic band structures of bP monolayer, MoS<sub>2</sub> monolayer, MoSe<sub>2</sub> monolayer, bP/MoS<sub>2</sub> and bP/MoSe<sub>2</sub> vdW heterostructures are shown in **Figure 2** (HSE06 method) and

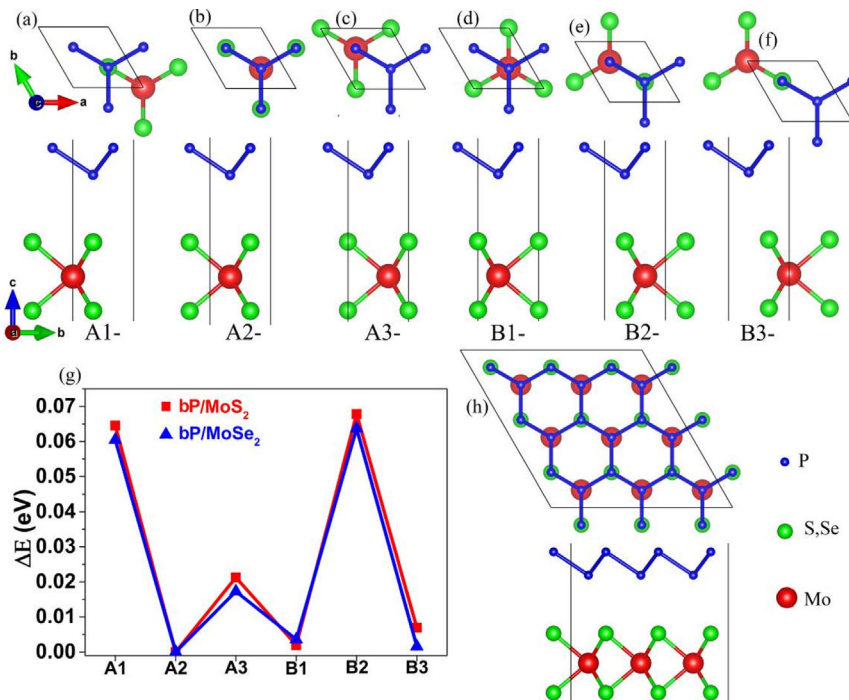


**Figure 1.** Six stacking structures of bP/MoS(Se)<sub>2</sub> heterostructures, (a)–(f) top and side views of A1-, A2-, A3-, B1-, B2-, and B3-stacking. g) Energy difference  $\Delta E_i$  (eV) between the energies of optimized bP/MoS(Se)<sub>2</sub> heterostructures and the most stable heterostructure (A2). h) Top and side views of the optimum stacking (A2-) order of the bP/MoS(Se)<sub>2</sub> heterostructures.

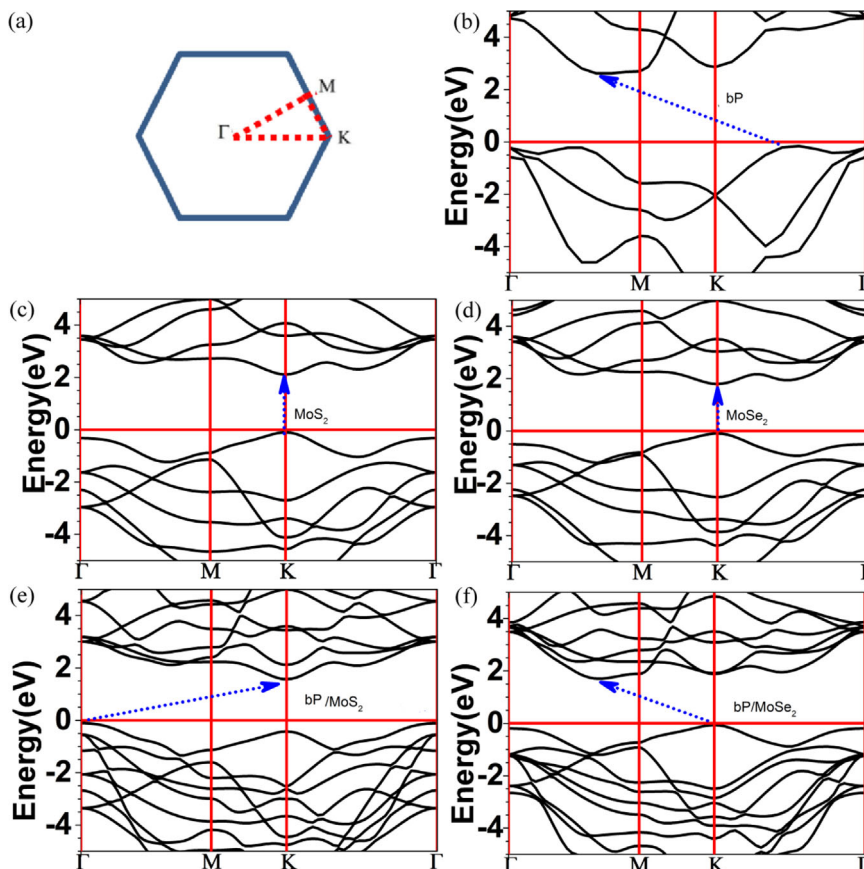


**Figure 2.** a) Brillouin zone with high-symmetry points labeled. Band structures (HSE06) of (b) bP monolayer, (c) MoS<sub>2</sub> monolayer, (d) MoSe<sub>2</sub> monolayer, (e) bP/MoS<sub>2</sub> vdW heterostructure and (f) bP/MoSe<sub>2</sub> vdW heterostructure.

Figure S1, Supporting Information (PBE method). Due to the improper treatment of the Coulomb repulsion, the band gaps from the GGA-PBE functionals are underestimated. In comparison, the band gaps based on the hybrid HSE06 method are enhanced. Except for the bigger band gaps, the electronic band structures based on HSE06 method computation are similar to those based on PBE method computation. As shown in Figure 2(b), bP monolayer was an indirect gap semiconductor with  $E_g$  of  $\approx 2.778$  eV. The valence band maximum (VBM) located between K and  $\Gamma$  points and the conduction band minimum (CBM) located between the  $\Gamma$  and M points. It was seen from Figure 2(c) and (d) that both MoS<sub>2</sub> and MoSe<sub>2</sub> monolayer were a direct gap semiconductor with  $E_g$  of  $\approx 2.208$  and 1.889 eV, respectively. Their VBMs and CBMs both located at the K point. The calculated electronic band structures of monolayer MoS<sub>2</sub>, MoSe<sub>2</sub>, and bP all agreed well with previous works.<sup>[9,15]</sup> As shown in Figure 2(e) and (f), the bP/MoS(Se)<sub>2</sub> vdW heterostructures, indirect gap semiconductor could be found, because of the band structures preserved both the properties of bP and MoS(Se)<sub>2</sub>. The  $E_g$  of bP/MoS<sub>2</sub> and bP/MoSe<sub>2</sub> vdW heterostructures were 1.677 and 1.769 eV, respectively. For the bP/MoS<sub>2</sub> vdW heterostructure, the VBM located at the  $\Gamma$  point but the CBM located at the K point. For the bP/MoSe<sub>2</sub> vdW heterostructure, the VBM located at the K point, while the CBM located between the  $\Gamma$  and M points. What is

more, the energy level of VBM at  $\Gamma$  point and K point were almost the same.

The planar average potential is shown in Figure 3 and Figure S2, Supporting Information. The energy of a stationary electron in the vacuum nearby the surface ( $E_{vac}$ ) of MoS<sub>2</sub>, MoSe<sub>2</sub>, bP, bP/MoS<sub>2</sub>, and bP/MoSe<sub>2</sub> were 2.459, 2.258, 1.807, 5.034, and 4.786 eV, respectively. The depth of electrostatic potential, from  $E_{vac}$  to the minimum of planar average potential, was 20.187, 15.317, and 19.747 eV for MoS<sub>2</sub>, MoSe<sub>2</sub>, and bP, respectively. The depth of the MoS<sub>2</sub> was close to the depth of bP. On the contrary, the difference between MoSe<sub>2</sub> and bP was obvious. These difference between MoS<sub>2</sub> (MoSe<sub>2</sub>) and bP would lead to a similar conclusion in the potential drop. For the bP/MoS<sub>2</sub> vdW heterostructure, the potential drop was about 0.839 eV (Figure 3 (a)) and the planar-averaged differential charge density across bP/MoS<sub>2</sub> slightly changed (Figure 3(b)). As shown in Figure 3(c), the decomposed charge density of the VBM and CBM of bP/MoS<sub>2</sub> vdW heterostructure indicated that Mo atom mainly contribute to the VBM and CBM. And the calculated band alignments of bP/MoS<sub>2</sub> vdW heterostructure is shown in Figure 3(d), indicating a type-I alignment. For the bP/MoSe<sub>2</sub> vdW heterostructure, the potential drop across bP/MoSe<sub>2</sub> was 4.208 eV (Figure 3(e)). A large potential difference for bP/MoSe<sub>2</sub> indicated that a large intrinsic electric field across the interface, where the electrons and holes were more easily separated or

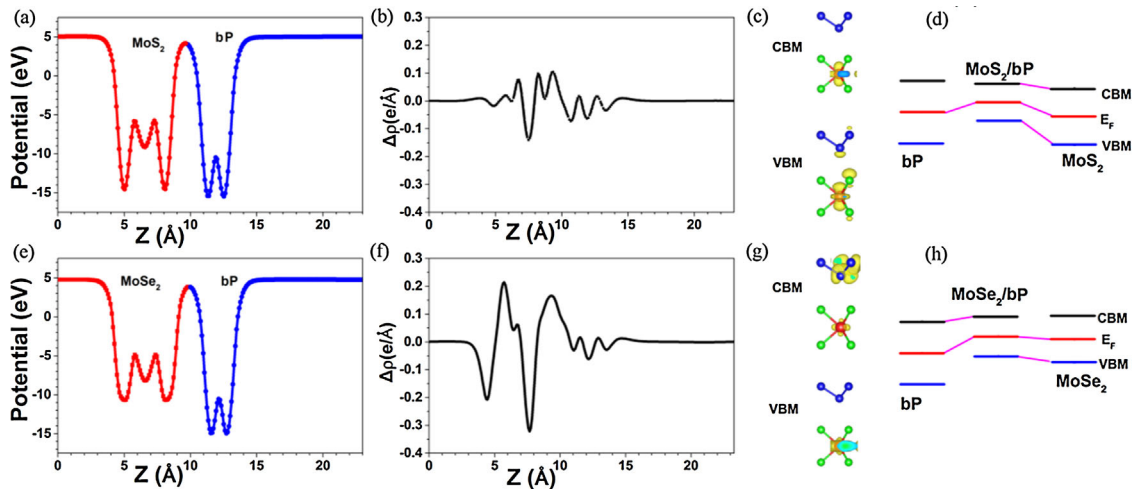


**Figure 3.** (a,e) The planar average potential, (b,f) the planar-averaged differential charge density, (c,g) the band decomposed charge density of the CBM and VBM, and (d,h) the Band alignments of bP/MoS<sub>2</sub> and bP/MoSe<sub>2</sub> vdW heterostructure, respectively.

transferred. The decomposed charge density of the VBM and CBM of bP/MoS<sub>2</sub> heterostructure indicated that Mo atom contributed to the VBM and P atom mainly contributed to the CBM, respectively (Figure 3(g)). As seen in Figure 3(h), the band edge positions of these vdW heterostructures were located between CBM of bP and VBM of MoSe<sub>2</sub> indicating a type-II heterostructure, which was important for application in photovoltaics and photodetection.

In-plane uniaxial strain and biaxial strain on the bP/MoS(Se)<sub>2</sub> vdW heterostructures were applied by changing the lattice parameters. Here, “-” represents compression and “+” represents stretching. As seen in Figure 4(a) and Figure S3 (a), Supporting Information the band gap values of the bP/MoS<sub>2</sub> vdW heterostructures were sensitive to the biaxial strain or uniaxial strain. The band gap values computed from HSE06 functionals are bigger than those from PBE functionals. However, the trends of the change of the band gaps of bP/MoS<sub>2</sub> vdW heterostructure in responding to the strain are concordant for both methods. Therefore, the band gaps predicted from HSE06 functionals were taken for example to analyze the trend of bP/MoS<sub>2</sub> vdW heterostructure as a function of biaxial strain. The band gap linearly decreased from 1.677 to 0.113 eV when the biaxial strain increased from 0 to +8%. When the biaxial strain was +10%, the band gap value was less than zero, which indicated bP/MoS<sub>2</sub> heterostructure had transferred from semiconductor to typically metallic and the transferred stretching strain is about 9%.

Moreover, when the biaxial strain decreased to -2%, the band gap reached the maximum  $\approx 2.149$  eV. It was worth noting that under the state of biaxial strain -2%, the lattice constants of bP/MoS<sub>2</sub> heterostructure was 3.159 Å closely to the lattice constants of the monolayer MoS<sub>2</sub> (3.169 Å). The band gap linearly decreased as the decrease of the biaxial strain from -2 to -10%. Especially, when the biaxial strain was -10%, the band gap value was less than zero, too, which indicated bP/MoS<sub>2</sub> heterostructure could also transfer from semiconductor to typically metallic under the compression and the transferred compressing strain is about -8.5%. The Figure 4(b) shown that

the conduction and valance band energies in the first Brillouin zone of bP/MoS<sub>2</sub> vdW heterostructure as functions of applied biaxial strain. All points except  $\Gamma_{\text{VBM}}$  possessed similar trend. The energy value of those symmetric points increased as the increase of biaxial strain from -10 to -2%. When the biaxial strain was -2%, they possessed the maximum value, and then they decreased as the increase of biaxial strain from -2 to 8%. The change of  $\Gamma_{\text{VBM}}$  was not obvious when the biaxial strain varied. It was worth noting that  $K_{\text{CBM}}$  was the minimum among the symmetric points of CBM and  $\Gamma_{\text{VBM}}$  was the maximum among the symmetric points of VBM indicating that the relative position of VBM and CBM were not changed. Moreover, when the biaxial strain was  $\pm 10\%$ , the  $K_{\text{CBM}}$  was less than Fermi energy and the  $\Gamma_{\text{VBM}}$  was slightly higher than Fermi energy level, which indicated bP/MoS<sub>2</sub> heterostructure had transferred from semiconductor to metallic. The detailed band structures (HSE06 and PBE) and projected densities of states (PBE) of the bP/MoS<sub>2</sub> vdW heterostructures at different biaxial strain were presented in Figure S4, Supporting Information. The details of band structures agreed well with the analysis above, especially the transformation from semiconductor to metallic was obvious. From the PDOS of the bP/MoS<sub>2</sub> vdW heterostructures, we could clearly see that when biaxial strain was 0%, it was *p*-orbitals of Mo and *s*-orbitals of S and P that contributed mainly to the VBM below Fermi level, while above the Fermi level, *p*-orbitals of Mo and *s*-orbitals of S contributed mainly to the CBM, indicating that bP/MoS<sub>2</sub> was a type-I heterostructure which coincided with the analysis of the band decomposed charge density and Band alignments mentioned above. When the biaxial strain was +8%, the *p*-orbitals of Mo shifted to Fermi level, while the biaxial strain was -8%, it was the *s*-orbitals of P that shifted to Fermi level obviously, which was the important reason for the emergence of metallic.

Similar to the bP/MoS<sub>2</sub> vdW heterostructures, the band gaps of bP/MoSe<sub>2</sub> vdW heterostructures could be widely tuned through uniaxial strain or biaxial strain. Specially, beyond a critical biaxial strain -12 or +14%, the transition from semiconductor to metal could be observed clearly (Figure 4(c))

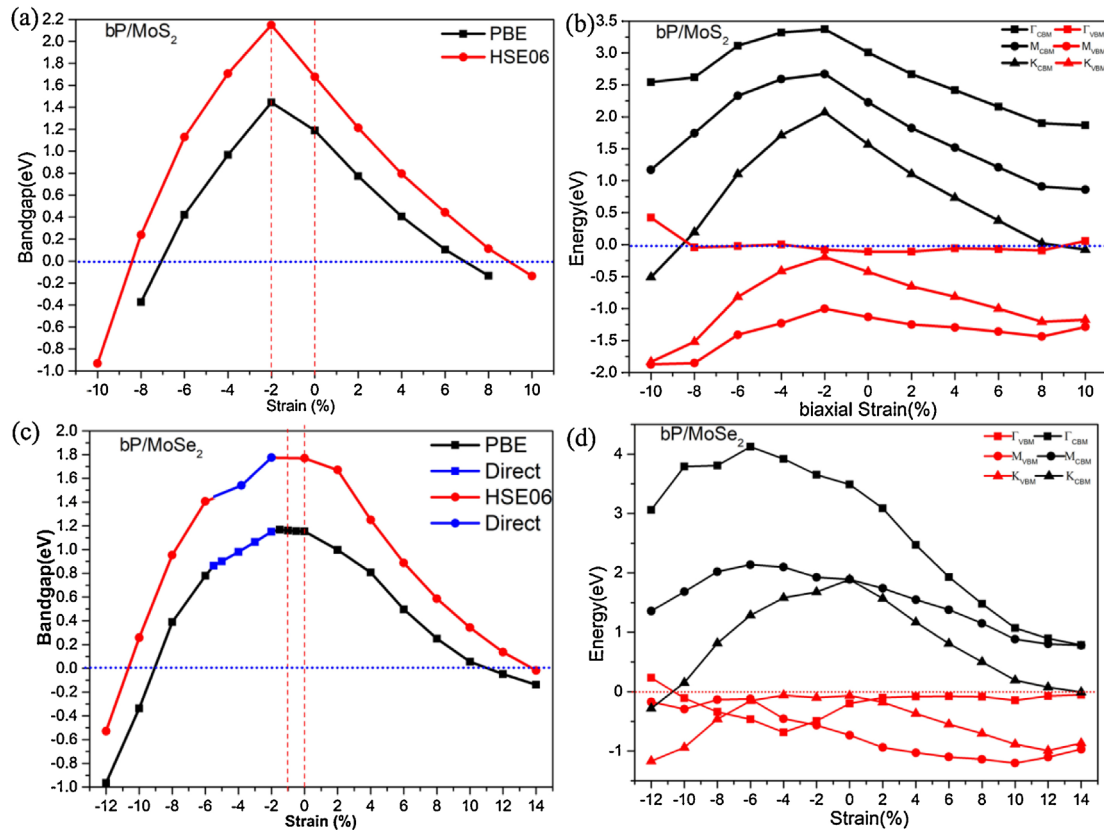


**Figure 4.** a) The band gap (HSE06 and PBE) of bP/MoS<sub>2</sub> vdW heterostructure as a function of biaxial strain. b) The conduction and valence band energies (HSE06) at different symmetry point in the first Brillouin zone of bP/MoS<sub>2</sub> vdW heterostructure as a function of biaxial strain. c) The band gap (HSE06 and PBE) of bP/MoSe<sub>2</sub> vdW heterostructure as a function of biaxial strain. d) The conduction and valence band energies (HSE06) at different symmetry point in the first Brillouin zone of bP/MoSe<sub>2</sub> vdW heterostructure as a function of biaxial strain.

and the transferred stretching and compressing strain are  $-10.5$  and  $13\%$ , respectively. Under the state of biaxial strain  $-1\%$ , the lattice constants of bP/MoSe<sub>2</sub> heterostructure was  $3.265 \text{ \AA}$  closely to the lattice constants of the monolayer bP ( $3.278 \text{ \AA}$ ), in this case, the band gap of bP/MoSe<sub>2</sub> vdW heterostructure reached the maximum value. What is more important, in the strain of  $-2$  to  $-5.5\%$  range, the system exhibits a direct band gap character, the VBM and CBM both locate at the  $K$  point. More details were shown in the conduction and valence band energies of the six points ( $\Gamma_{\text{VBM}}$ ,  $M_{\text{VBM}}$ ,  $K_{\text{VBM}}$ ,  $\Gamma_{\text{CBM}}$ ,  $M_{\text{CBM}}$ , and  $K_{\text{CBM}}$ ) as functions of applied biaxial strain. As shown in Figure 4 (d), within the strain range of  $0$ – $10\%$ , all points except  $\Gamma_{\text{VBM}}$  reduced as the biaxial strain increased, yet the  $\Gamma_{\text{VBM}}$  was stable without obvious change. The change in the  $0$  to  $-6\%$  was more complicated and important. It was worth noting that when the biaxial strain was  $0\%$ ,  $M_{\text{CBM}}$  was the minimum and  $K_{\text{CBM}}$  was just slightly larger than  $M_{\text{CBM}}$ , while the biaxial strain was in the range of  $-2$  to  $-10\%$ , the  $K_{\text{CBM}}$  dramatically reduced to be the minimum. On the contrast, the  $K_{\text{VBM}}$  kept stable without obvious change to be the maximum during the  $-2$  to  $-5.5\%$  range. So the system exhibits a direct band gap in the range of  $-2$  to  $-5.5\%$ . Moreover, when the biaxial strain was  $-12$  or  $+14\%$  the  $K_{\text{CBM}}$  was less than Fermi energy level and the  $\Gamma_{\text{VBM}}$  was slightly higher than Fermi energy level, which indicated bP/MoSe<sub>2</sub> heterostructure had changed from semiconductor to

typically metallic. The detailed band structures (HSE06 and PBE) and projected densities of states (PBE) of the bP/MoSe<sub>2</sub> vdW heterostructures at different biaxial strain were presented in Figure S5, Supporting Information. From the band structures of the bP/MoSe<sub>2</sub> vdW heterostructures, the change of the conduction and valence band energies of the six points could be observed clearly, especially an intriguing transition from indirect to direct and from semiconductor to metal. From the PDOS of the bP/MoSe<sub>2</sub> vdW heterostructures, we could clearly see that when biaxial strain was  $0\%$ , it was  $p$ -orbitals of Mo and  $s$ -orbitals of Se and P that contributed mostly to the VBM below Fermi level, while above the Fermi level,  $p$ -orbitals of Mo and  $s$ -orbitals of Se contributed mostly to the CBM, indicating that bP/MoSe<sub>2</sub> was a type-II heterostructure which was useful photovoltaic devices and photocatalytic due to the desirable characteristic of efficient electron-hole separation. As biaxial strain increased, the orbitals of CBM, including  $p$ -orbitals of Mo and  $s$ -orbitals of Se, gravitated to Fermi level and the band gap reduced progressively. At  $+10\%$  biaxial strain, the orbitals of CBM across Fermi level led to the change from semiconductor to metallic. Within the  $0\%$ – $2\%$  range of biaxial strain, the orbitals of CBM kept away from the Fermi level, which coincided with the enlargement of band gap. As biaxial strain decreased from  $-2$  to  $-10\%$ ,  $p$ -orbitals of P, which contributed mostly to the CBM, gravitated to Fermi level and the band gap reduced

progressively. At  $-10\%$  biaxial strain, the orbitals of CBM across Fermi level led to the change from semiconductor to metallic. Therefore, theoretical predictions suggest that the bP/MoSe<sub>2</sub> vdW heterostructures are very promising for optoelectronic applications due to their tunable band gaps by applying strain.

The absorption coefficient was an important factor for photoelectronic devices and solar cells. The perfect devices should absorb visible light and UV light as much as possible. However, the previous paper reported that MoS(Se)<sub>2</sub> single layer exhibited light absorption mainly in the visible light region, while the bP single layer exhibited light absorption only in the UV light region.<sup>[34]</sup> As shown in Figure 5, bP/MoS(Se)<sub>2</sub> heterostructures exhibit strong visible–UV light absorption in the wavelength range of 50–800 nm, especially the 60–300 nm, indicating that bP/MoS(Se)<sub>2</sub> heterostructures could break the limitation of a single layer and combine together the advantageous properties of different layers. The reasons for this optical absorption phenomenon vdW heterostructures were understandable, including that the interlayer coupling, the electronic states overlapping and charge transfer in the heterostructures, where the new optical transitions were induced.<sup>[35]</sup> This interesting phenomenon was also found in the black (blue) phosphorus/g-ZnO vdW heterostructures.<sup>[35]</sup> In addition, the absorption coefficients of bP/MoS(Se)<sub>2</sub> heterostructures about  $10^5$ – $10^6$  cm<sup>-1</sup> under visible–UV light, which are stronger than that of black(blue)-P/g-ZnO hetero-junction (about  $10^4$  cm<sup>-1</sup>),<sup>[35]</sup> are similar to the absorption

coefficients of InSe/SnS and InSe/GeSe heterojunctions.<sup>[36]</sup> Furthermore, as shown in Figure 5(a) and (c), red shift has taken place at its absorption edge as the biaxial strain increased. While the absorption coefficients increased as the biaxial strain decreased. From Figure S6, Supporting Information the relationship between absorption edge, optical energy gap and biaxial strain were obvious, especially the optical energy gap were sensitive to the biaxial strain. The optical energy gap change curves coincided with the band gap of bP/MoS(Se)<sub>2</sub> vdW heterostructure as a function of strain mentioned above, indicating that it was effective to tune the optical properties of bP/MoS(Se)<sub>2</sub> vdW heterostructures via biaxial strain, therefore, these theoretical predictions suggest that bP/MoS(Se)<sub>2</sub> heterostructures are promising visible–ultraviolet optoelectronic applications due to their tunable electronic and optical properties.

In conclusion, the strain-engineering of the structural, energetic, electronic, and optical properties of the bP/MoS(Se)<sub>2</sub> heterostructures have been performed by means of high-fidelity first-principles calculations, including uniaxial strain and biaxial strains. The bP/MoS(Se)<sub>2</sub> vdW heterostructures exhibited indirect gap characteristics. The band gap values were sensitive to the in-plane strain. Specially, for bP/MoSe<sub>2</sub> heterostructure system, biaxial compressive strain range of  $-2$  to  $-5.5\%$  could induce the modulation of direct band gap character with the VBM and CBM both located at the K point. However, bP/MoS<sub>2</sub> heterostructures do not exhibit a direct band gap under uniaxial

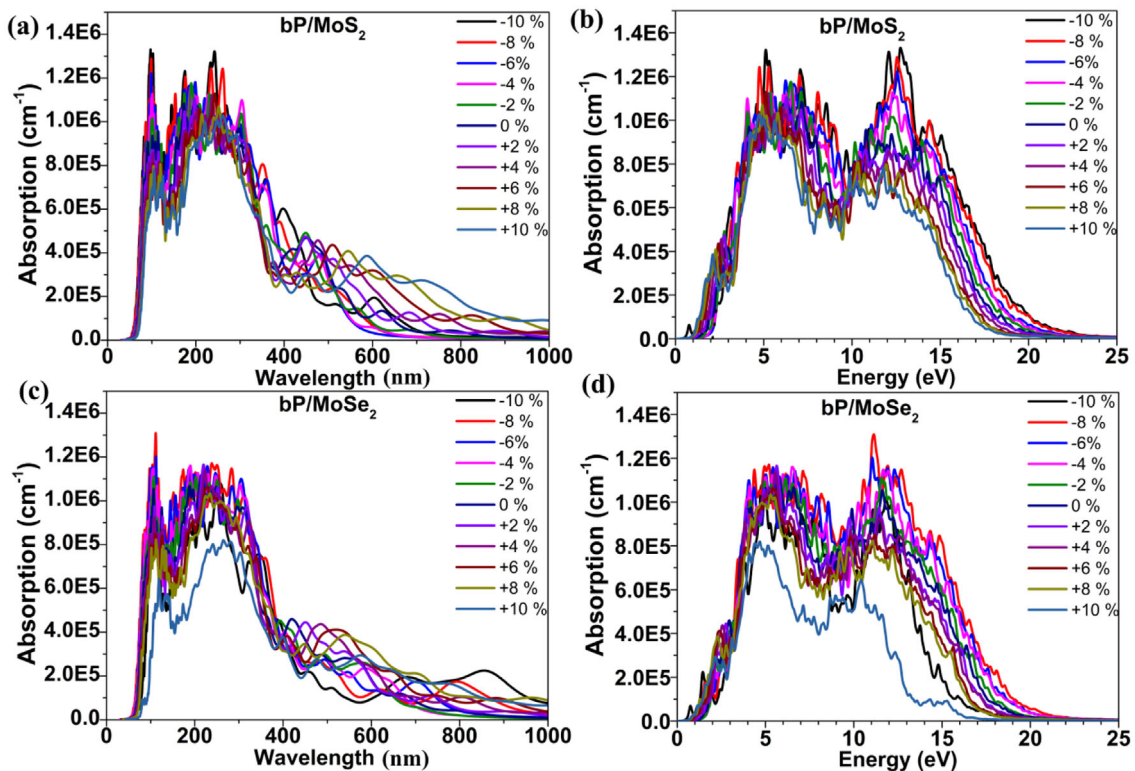


**Figure 5.** Absorption coefficients of (a,b) bP/MoS<sub>2</sub> and (c,d) bP/MoSe<sub>2</sub>. Panels (a,c) and (b,d) are absorption coefficient versus wavelength and energy, respectively.

strain. What is more, there are two critical strains of  $-0.085$  ( $-0.105$ ) and  $+0.09$  ( $+0.135$ ) for bP/MoS(Se)<sub>2</sub> heterostructures, where the semiconductor-metal transition could be observed. Moreover, the bP/MoS(Se)<sub>2</sub> heterostructures exhibited strong visible–UV light absorption in the wavelength range of 50–800 nm, and it was effective to tune and enhance the optical properties of bP/MoS(Se)<sub>2</sub> vdW heterostructures via biaxial strain. Therefore, these theoretical predictions suggest that bP/MoS(Se)<sub>2</sub> heterostructures are promising excellent visible-ultraviolet optoelectronic applications due to their tunable electronic and optical properties.

## Experimental Section

The present calculations were performed using the Vienna ab initio simulation package (VASP)<sup>[37]</sup> in conjunction with the projector-augmented-wave (PAW) potential.<sup>[38]</sup> The Perdew–Burke–Ernzerhof (PBE) functional of the generalized gradient approximation (GGA) was used to describe the exchange–correlation energy.<sup>[39]</sup> The HSE06 hybrid functional<sup>[40]</sup> was adopted to calculate more accurate band gaps. In order to better take into account the vdW forces between monolayer MoS(Se)<sub>2</sub> and monolayer bP, the van der Waals density functional of optB88<sup>[41–43]</sup> was considered in all calculations to give an improved description for bP/MoS(Se)<sub>2</sub> vdW heterostructures. The energy cutoff for the plane-wave expansion of the wave function was set to 400 eV. All the structures were fully relaxed until satisfying an energy convergence of  $10^{-4}$  eV and the maximum Hellmann Feynman force convergence of  $0.01$  eV Å<sup>-1</sup>. The Gamma center scheme was used for the first Brillouin zone integration with a fine grid of  $9 \times 9 \times 1$  and  $12 \times 12 \times 1$  for structure optimization and static calculation,<sup>[44]</sup> respectively. The thickness of the vacuum region along the z direction was more than 15 Å to eliminate the artificial interactions due to the periodic image.

## Supporting Information

Supporting Information is available from the Wiley Online Library or from the author.

The supplementary figures (Figure S1–S6) display the electronic band structures, planar average potentials, PBE bandgap tuning, band structures at  $-10$ ,  $-2$ ,  $0$ ,  $10\%$ , and absorption coefficients of bP/MoS(Se)<sub>2</sub>, respectively. All data generated or analyzed during this study are included in this published article and its Supporting Information file.

## Acknowledgment

Authors acknowledge the financial support from National Natural Science Foundation of China (11464001).

## Author Contributions

Y.O. and Q.P. designed the project. D.G., X.T., H.C., and W.Z. carried out the simulations. D.G., X.T., Y.D., and Y.O. did the analysis. Y.O. and Q.P. wrote the paper. All authors discussed and commented on the manuscript.

## Conflict of Interest

The authors declare no conflict of interest.

## Keywords

blue phosphorene, MoS<sub>2</sub>, MoSe<sub>2</sub>, strain engineering, ultraviolet absorption, van der Waals heterostructures

Received: December 11, 2018

Revised: January 4, 2019

Published online: January 23, 2019

- [1] K. S. Novoselov, A. K. Geim, S. V. Morozov, D. Jiang, Y. Zhang, S. V. Dubonos, I. V. Grigorieva, A. A. Firsov, *Science* **2004**, *306*, 666.
- [2] K. S. Novoselov, *Angew. Chem. Int. Ed.* **2011**, *50*, 6986.
- [3] Q. Peng, S. De, *Phys. E* **2012**, *44*, 1662.
- [4] Y. G. Li, Y. L. Li, C. M. Araujo, W. Luo, R. Ahuja, *Catal. Sci. Technol.* **2013**, *3*, 2214.
- [5] K. F. Mak, C. Lee, J. Hone, J. Shan, T. F. Heinz, *Phys. Rev. Lett.* **2010**, *105*, 136805.
- [6] Q. Peng, S. De, *Phys. Chem. Chem. Phys.* **2013**, *15*, 19427.
- [7] Q. H. Wang, K. Kalantar-Zadeh, A. Kis, J. N. Coleman, M. S. Strano, *Nat. Nanotechnol.* **2012**, *7*, 699.
- [8] S. Lebegue, O. Eriksson, *Phys. Rev. B* **2009**, *79*, 115409.
- [9] Y. Ding, Y. Wang, J. Ni, L. Shi, S. Shi, W. Tang, *Physica B* **2011**, *406*, 2254.
- [10] T. Korn, S. Heydrich, M. Hirmer, J. Schmutzler, C. Schüller, *Appl. Phys. Lett.* **2011**, *99*, 102109.
- [11] H. Liu, A. T. Neal, Z. Zhu, Z. Luo, X. Xu, D. Tomanek, P. D. Ye, *ACS Nano* **2014**, *8*, 4033.
- [12] E. S. Reich, *Nature* **2014**, *506*, 19.
- [13] Z. Zhu, D. Tomanek, *Phys. Rev. Lett.* **2014**, *112*, 176802.
- [14] C. Wang, Q. He, U. Halim, Y. Liu, E. Zhu, Z. Lin, H. Xiao, X. Duan, Z. Feng, R. Cheng, N. O. Weiss, G. Ye, Y. C. Huang, H. Wu, H. C. Cheng, I. Shakir, L. Liao, X. Chen, W. A. Goddard III, Y. Huang, X. Duan, *Nature* **2018**, *555*, 231.
- [15] X. Zhu, T. Zhang, D. Jiang, H. Duan, Z. Sun, M. Zhang, H. Jin, R. Guan, Y. Liu, M. Chen, H. Ji, P. Du, W. Yan, S. Wei, Y. Lu, S. Yang, *Nat. Commun.* **2018**, *9*, 4177.
- [16] B. Ghosh, S. Nahas, S. Bhowmick, A. Agarwal, *Phys. Rev. B* **2015**, *91*, 115433.
- [17] J. L. Zhang, S. Zhao, C. Han, Z. Wang, S. Zhong, S. Sun, R. Guo, X. Zhou, C. D. Gu, K. D. Yuan, Z. Li, W. Chen, *Nano Lett.* **2016**, *16*, 4903.
- [18] D. Tristant, A. Cupo, V. Meunier, *2D Mater.* **2018**, *5*, 035044.
- [19] J. Zhuang, C. Liu, Q. Gao, Y. Liu, H. Feng, X. Xu, J. Wang, J. Zhao, S. X. Dou, Z. Hu, Y. Du, *ACS Nano* **2018**, *12*, 5059.
- [20] J. Xiao, M. Long, X. Zhang, J. Ouyang, H. Xu, Y. Gao, *Sci. Rep.* **2015**, *5*, 9961.
- [21] A. K. Geim, I. V. Grigorieva, *Nature* **2013**, *499*, 419.
- [22] Q. Li, J. Yang, L. Zhang, *J. Phys. Chem. C* **2018**, *122*, 18294.
- [23] S. Wang, C. Ren, H. Tian, J. Yu, M. Sun, *Phys. Chem. Chem. Phys.* **2018**, *20*, 13394.
- [24] V. O. Ozcelik, J. G. Azadani, C. Yang, S. J. Koester, T. Low, *Phys. Rev. B* **2016**, *94*, 035125.
- [25] Z. Guo, N. Miao, J. Zhou, B. Sa, Z. Sun, *J. Mater. Chem. C* **2017**, *5*, 978.
- [26] Y. C. Huang, X. Chen, C. Wang, L. Peng, Q. Qian, S. F. Wang, *Nanoscale* **2017**, *9*, 8616.
- [27] W. Li, T. Wang, X. Dai, Y. Ma, Y. Tang, *J. Alloys Compd.* **2017**, *705*, 486.
- [28] Q. Yang, C.-J. Tan, R.-S. Meng, J.-K. Jiang, Q.-H. Liang, X. Sun, D.-G. Yang, X.-P. Chen, *IEEE Electron Device Lett.* **2017**, *38*, 145.
- [29] W. C. Yap, Z. Yang, M. Mehboudi, J.-A. Yan, S. Barraza-Lopez, W. Zhu, *Nano Res.* **2017**, *11*, 420.

- [30] Y. Deng, Z. Luo, N. J. Conrad, H. Liu, Y. Gong, S. Najmaei, P. M. Ajayan, J. Lou, X. Xu, P. D. Ye, *ACS Nano* **2014**, *8*, 8292.
- [31] V. D. S. O. Ganesan, J. Linghu, C. Zhang, Y. P. Feng, S. Lei, *Appl. Phys. Lett.* **2016**, *108*, 122105.
- [32] L. Huang, Y. Li, Z. Wei, J. Li, *Sci. Rep.* **2015**, *5*, 16448.
- [33] Z. Y. Zhang, M. S. Si, S. L. Peng, F. Zhang, Y. H. Wang, D. S. Xue, *J. Solid State Chem.* **2015**, *231*, 64.
- [34] Q. Peng, Z. Wang, B. Sa, B. Wu, Z. Sun, *Sci. Rep.* **2016**, *6*, 31994.
- [35] W. Zhang, L. Zhang, *RSC Adv.* **2017**, *7*, 34584.
- [36] C.-x. Xia, J. Du, X.-w. Huang, W.-b. Xiao, W.-q. Xiong, T.-x. Wang, Z.-m. Wei, Y. Jia, J.-j. Shi, J.-b. Li, *Phys. Rev. B* **2018**, *97*, 115416.
- [37] G. Kresse, J. Furthmüller, *Phys. Rev. B* **1996**, *54*, 11169.
- [38] P. E. Blochl, *Phys. Rev. B: Condens. Matter* **1994**, *50*, 17953.
- [39] J. P. Perdew, K. Burke, M. Ernzerhof, *Phys. Rev. Lett.* **1996**, *77*, 3865.
- [40] J. Paier, M. Marsman, K. Hummer, G. Kresse, I. C. Gerber, J. G. Angyan, *J. Chem. Phys.* **2006**, *124*, 154709.
- [41] A. D. Becke, *Phys. Rev. A: Gen. Phys.* **1988**, *38*, 3098.
- [42] J. Klimes, D. R. Bowler, A. Michaelides, *J. Phys.: Condens. Matter* **2010**, *22*, 022201.
- [43] J. Klimeš, D. R. Bowler, A. Michaelides, *Phys. Rev. B* **2011**, *83*, 195131.
- [44] H. J. Monkhorst, J. D. Pack, *Phys. Rev. B* **1976**, *13*, 5188.